Visible-Light-Induced Photodegradation of Methylene Blue Using Mn,N-codoped $ZrTiO_4$ as Photocatalyst

Akhmad Syoufian[1*] and Rian Kurniawan[2]

[1]*Department of Chemistry, Faculty of Mathematics and Natural Sciences, Universitas Gadjah Mada, Sekip Utara, Yogyakarta 55281, Indonesia*

[2]*Institute of Chemical Technology, Universität Leipzig, Linnéstr. 3, 04103 Leipzig, Germany*

* ***Corresponding author:***

email: akhmadsyoufian@ugm.ac.id

Received: November 19, 2022
Accepted: April 3, 2023

DOI: 10.22146/ijc.79261

Abstract: *Composites of manganese and nitrogen-codoped zirconium titanate (Mn,N-codoped $ZrTiO_4$) had been synthesized by the sol-gel method as a visible-light responsive photocatalyst for the photodegradation of methylene blue (MB). Synthesis was conducted at 25 °C using titanium(IV) isopropoxide, zirconium oxide, urea, and manganese(II) chloride. Mn,N-codoped $ZrTiO_4$ containing fixed 10% nitrogen dopant (w_N/w_{Ti}) with various Mn dopant contents (2, 4, 6, 8, and 10% w_{Mn}/w_{Ti}) and calcination temperatures (500, 700, and 900 °C) had been investigated. All of the Mn,N-codoped $ZrTiO_4$ exhibit a band gap within the visible range (2.51 to 2.74 eV). Photodegradation of MB was performed under visible light illumination for 120 min. The highest activity was achieved up to 7.7 μg L^{-1} min^{-1}, which was obtained from Mn,N-codoped $ZrTiO_4$ calcined at 500 °C containing 6% Mn and 10% N dopants.*

Keywords: *Mn,N-codoped $ZrTiO_4$; band gap; methylene blue; photodegradation; visible-light*

■ INTRODUCTION

Methylene blue (MB) is a synthetic dye and is widely used in the textile, pharmaceutical, paper, printing, paint, and food industries [1]. MB is an azo dye that will form quaternary ammonium cation when dissolved in water and has a high chrome content [2]. The presence of MB in the environment can cause various negative impacts, such as reducing the transmission of sunlight and solubility of oxygens, affecting photosynthetic activity in the aquatic ecosystem, which also reduces the diversity, and decreases the aesthetics of the ecosystem [3]. Due to the high aromatic content and stability properties of MB, biological treatment is not effective in degrading the dye. This ineffectiveness is associated with the presence of azo compounds, which are resistant to aerobic and anaerobic degradations. When azo is reduced, it will produce colorless aromatic amine compounds, which are potentially carcinogenic [4-5]. The development of technology for MB removal with a total contaminant destruction system is necessary. Therefore, the oxidation of MB to H_2O and CO_2 via photocatalysis is an interesting subject to study.

The photodegradation process can occur in the presence of a photocatalyst, i.e., a semiconductor that can be activated by absorbing photons and accelerating a reaction without being consumed. By absorbing photons with energy equal to or greater than the semiconductor band gap, photocatalysis is carried out on the semiconductor photocatalyst to produce an electron-hole [6]. The photo-induced electrons and holes react with oxygen, water, and hydroxyl group to generate reactive oxygen species, such as hydroxyl radicals (•OH) and superoxide radical anions ($•O_2^-$) with strong oxidation abilities [7]. The weaknesses of a semiconductor photocatalyst are its limit of application, such as low usage in visible light, wide band gap, and high recombination rate of photo-induced electrons and holes [8]. Therefore, various elements, such as noble metals and transition metals, as well as non-metals and metalloids, are doped into the photocatalyst to enhance the photodegradation performance [9].

Titanium oxide or titania (TiO_2) is widely used as a photocatalyst because of its attractive properties, such as non-toxicity, low cost, strong oxidizing, and biological and chemical inertness [10]. TiO_2 has broad band gaps, 3.0 eV for the rutile phase and 3.2 eV for the anatase phase, which causes limited light absorption, thus making TiO_2 effective as a photocatalyst in spectrum ultraviolet region (4–5% of solar light) and very low activity in visible light (~45% of solar spectrum) [11]. Therefore, previous research has reported visible-light-active TiO_2 by incorporating different dopants, which involve metal (Mn, Fe, and Ni) [12-15] and non-metal (C, N, F, and S) [16-21]. The metal dopant can improve the separation of electrons and holes on the surface of the photocatalyst. Another semiconductor, such as zirconium oxide or zirconia (ZrO_2), has very limited photocatalytic properties, but the addition of another oxide, such as TiO_2, ZnO and SnO_2, has a beneficial effect on their photocatalytic activity [22]. The addition of ZrO_2 into TiO_2 in $ZrTiO_4$ composite can increase the surface area because ZrO_2 inhibits the phase transition of anatase to rutile and crystallite growth in TiO_2 [23].

In this work, manganese and nitrogen codoped $ZrTiO_4$ composites were prepared by the sol-gel method. The sol-gel method was chosen because it has numerous benefits, such as a simple synthesis process at ambient temperature under atmospheric pressure, does not require a complicated setup, low cost, and is eco-friendly [24]. TiO_2 was grown on the surface of ZrO_2 to form a material with higher thermal stability. Both metal and nonmetal dopants, i.e., Mn and N, were incorporated into the $ZrTiO_4$ to enhance the photodegradation ability of the material in visible light. Mn was selected as a dopant due to its photocatalytic-activity improvement to TiO_2 in visible-light region and its similar six-fold ionic radius to Ti ion (Mn^{4+} = 0.53 Å; Ti^{4+} = 0.60 Å) [12]. Meanwhile, nitrogen was also selected as a dopant because it reduces the recombination rate of photogenerated charges in TiO_2 and shifts the light absorption ability of TiO_2 to the visible-light region, thus improving the photocatalytic activity as well [17]. Codoping, both Mn and N into $ZrTiO_4$, should further elevate the photocatalytic activity of the composite. Various Mn dopant contents and calcination temperatures were applied to understand the influence of Mn,N codoping and crystal structure on the photocatalytic activity of the $ZrTiO_4$ composite.

■ EXPERIMENTAL SECTION

Materials

Titanium(IV) tetraisopropoxide (TTIP) (97%, Sigma Aldrich) and ZrO_2 powder (Jiaozou Huasu) were chosen as TiO_2 precursor and supporting material, respectively. Manganese(II) chloride ($MnCl_2{\cdot}4H_2O$) (Merck) and urea (CH_4N_2O) (PA, Merck) were chosen as the dopant sources. Methylene blue (MB) (Thermo Fisher Scientific India Pvt. Ltd.) was used as a test dye for a photodegradation experiment to determine the activity of composites. Absolute ethanol (PA, Merck) and demineralized water (Jaya Sentosa) were used as solvents.

Instrumentation

Fourier transform infrared spectrophotometer (FTIR) Thermo Nicolet iS10 was used to identify the vibrational spectra of functional groups in the materials. The crystalline structure of the materials was analyzed using an X-ray powder diffractometer (XRD) Analytical X'Pert PRO MRD with Cu Kα radiation (λ = 1.54 Å, 40 kV, 30 mA). The morphology of the materials was observed by using a scanning electron microscope equipped with an energy-dispersive X-ray spectrometer (SEM-EDX) JSM-6510LA. The band gap of materials was determined from the absorption spectra using specular reflectance UV-Vis spectrometer (SR-UV) Shimadzu UV-1700 Pharmaspec. The concentration of MB was measured using a spectrophotometer UV-Vis Thermo Scientific Genesys 50.

Procedure

Synthesis and characterization of Mn,N-codoped $ZrTiO_4$

Mn,N-codoped $ZrTiO_4$ was synthesized by the sol-gel method at room temperature. TTIP as Ti precursor (2.5 mL) was dissolved in 25 mL of absolute ethanol and stirred for 10 min. Various amounts of $MnCl_2{\cdot}4H_2O$ (2, 4, 6, 8, and 10% (w_{Mn}/w_{Ti})), 1 g of ZrO_2, and 86.6 mg of urea (10% (w_N/w_{Ti})) were mixed in 25 mL of

demineralized water. The aqueous suspension was added to the TTIP solution dropwise under mild stirring. Then, the mixture was stirred for 30 min and then separated by centrifugation at 2000 rpm for 1 h. The solid was aged in the air for 48 h before being heated at 80 °C for 24 h. Composites with various Mn contents were calcined at 500 °C for 4 h under atmospheric conditions. Additionally, a composite with 6% of Mn content was calcined at 700 and 900 °C to observe the effect of calcination temperature. The composites are labeled as xMn-N-ZT-y, where x is the percentage of Mn content and y is the calcination temperature (°C). All composites were characterized using XRD, FTIR, SRUV, and SEM-EDX.

Photodegradation of methylene blue

About 15 mg of Mn,N-codoped $ZrTiO_4$ were added into 30 mL of 4 mg L^{-1} aqueous MB solution. The mixture was stirred under visible light irradiation for 120 min. Photodegradation of MB in visible light irradiation has been investigated using a LIFE MAX 30W/765 PHILIPS TLD Lamp. After the photodegradation process, the photocatalyst was separated by centrifugation. For comparison, the same procedure was also done for TiO_2 and ZrO_2. The concentration of MB after photodegradation was determined by a UV-Visible spectrophotometer at the optimum wavelength of the MB solution (664 nm). Quantitative analysis of the photodegradation was calculated using the pseudo-first kinetic order model (Eq. (1) and (2)):

$$-\frac{dC}{dt} = k_{obs}C \quad (1)$$

$$\ln C = -k_{obs}t + \ln C_0 \quad (2)$$

where k_{obs} is the observed rate constant for the photodegradation, C is the concentration of MB after degradation, C_0 is the initial concentration of MB, and t is the irradiation time [25]. The percentage of MB degradation was calculated following this calculation (Eq. (3)):

$$\%\text{MB degradation} = \frac{C_i - C_f}{C_i} \times 100\% \quad (3)$$

where C_i and C_f are the initial and the final concentration of MB (mg L^{-1}), respectively [26].

■ RESULTS AND DISCUSSION

The morphology of the composites was characterized by SEM-EDX. SEM images of ZrO_2, TiO_2, and 6Mn-N-ZT-500 composite are shown in Fig. 1. The surface of 6Mn-N-ZT-500 appears to be rougher and coarser than pure TiO_2 and ZrO_2, which indicates the deposition of TiO_2 on the ZrO_2 surface. Agglomeration is also formed in 6Mn-N-ZT-500 due to dopant incorporation. For higher dopant concentrations, agglomeration of dopant ions takes place at isolated locations, and thus surface starts charging [27]. There is no formation of any nanostructure-like nanorods or nanowires. It was also reported that the incorporation of dopants with different concentrations plays an important role in surface morphology [28].

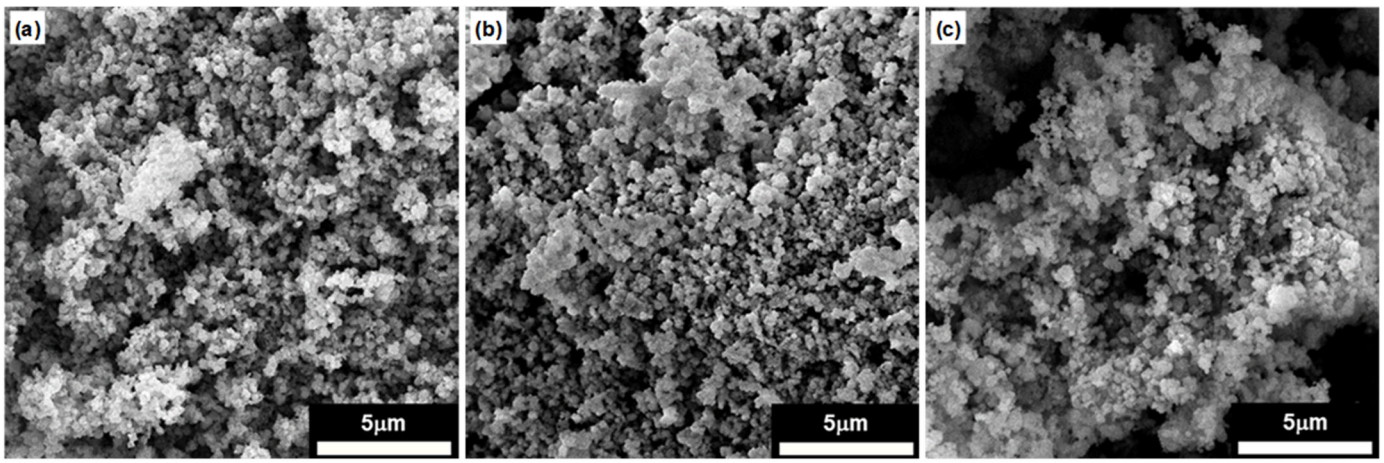

Fig 1. SEM images of (a) TiO_2 500 °C, (b) ZrO_2 500 °C and (c) 6Mn-N-ZT-500

The elemental mass percentage on the localized surface of the taken SEM images is summarized in Table 1. Manganese (Mn) was detected on the surface of the 6Mn-N-ZT-500, confirming the successful Mn doping. On the other hand, nitrogen (N) was not detected. It is possible that the amount of N was too low, so the amount of energy given off by X-rays after hitting the surface will be insufficient to adequately measure its proportion. Also, some elements are not easily detected (i.e., nitrogen, boron, and beryllium), and others (i.e., hydrogen, helium, and lithium) are not detectable at all, leading at times to materials misidentification due to low atomic number [29-30].

The diffraction pattern of Mn,N-codoped $ZrTiO_4$ with various Mn contents is shown in Fig. 2. Diffraction patterns of all Mn-N-ZT-500 display anatase and tetragonal structure but no rutile structure. Reflexes observed at 2θ = 25° (101) and 48° (200) correspond to the anatase TiO_2 pattern according to ICDD: 00-001-0562, while reflexes observed at 2θ = 30° (101) and 51° (112) correspond to tetragonal ZrO_2 pattern according to ICDD: 01-079-1763. The absence of rutile is possibly caused by the presence of ZrO_2, which can prevent the transformation of anatase to rutile in the TiO_2 structure. No shift of pattern is observed as the Mn content increases.

Reflexes of anatase (101) and tetragonal (101) were chosen as a comparison for average crystallite size (D). The crystallite size was calculated using Scherrer's equation [31]. Table 2 summarizes the calculated crystallite size of various Mn-N-ZT-500. No significant change is observed in both the crystallite size of anatase and tetragonal as the amount of Mn dopant increases. Mn doping causes no alteration to the crystal structure of

Table 1. Elemental surface composition of TiO_2 500 °C, ZrO_2 500 °C, and 6Mn-N-ZT-500

Material	% Mass					
	Zr	Ti	O	Mn	N	Total
TiO_2 500 °C	-	50.60	49.40	-	-	100
ZrO_2 500 °C	71.46	-	28.54	-	-	100
6Mn-N-ZT-500	31.35	29.58	38.35	0.72	-	100

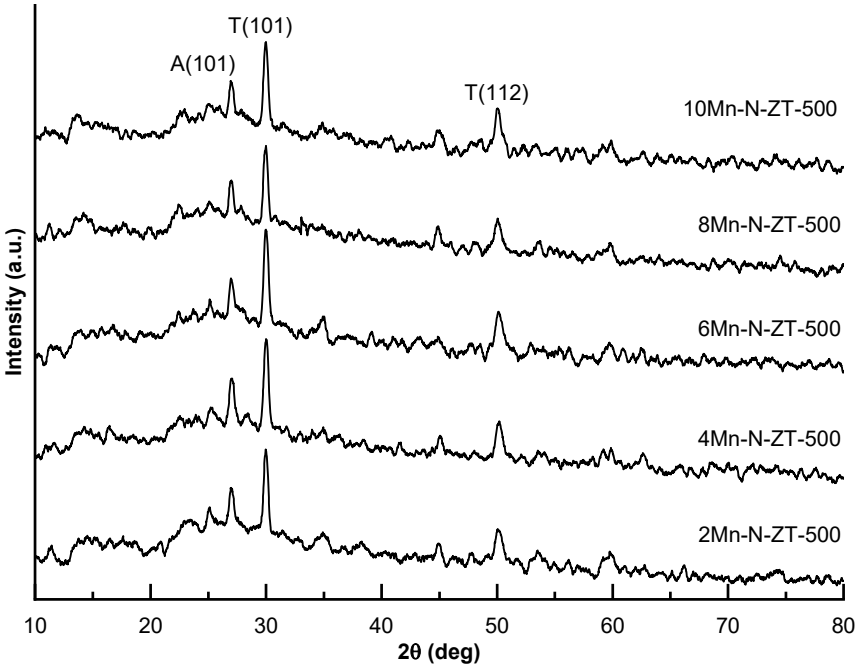

Fig 2. Diffraction patterns of Mn,N-codoped $ZrTiO_4$ with various Mn contents whereas A and T represent anatase and tetragonal crystal phases

Table 2. Crystal phase of various dopant Mn in composites

Material	Crystal phase	D (nm)
2Mn-N-ZT-500	Anatase	24
	Tetragonal	26
4Mn-N-ZT-500	Anatase	22
	Tetragonal	24
6Mn-N-ZT-500	Anatase	27
	Tetragonal	23
8Mn-N-ZT-500	Anatase	24
	Tetragonal	25
10Mn-N-ZT-500	Anatase	25
	Tetragonal	24

Mn,N-codoped $ZrTiO_4$. The amount of Mn-doped into Mn-N-ZT was too low, therefore, no changes can be detected properly by the X-ray powder diffraction.

Diffraction patterns of 6Mn-N-ZT calcined at 700 and 900 °C are displayed in Fig. 3. Both 6Mn-N-ZT-700 and 6Mn-N-ZT-900 exhibit rutile patterns in TiO_2 structure. A reflex at $2\theta = 27°$ (110) corresponds to rutile TiO_2 according to ICDD: 03-065-1118. The intensity of the anatase reflex is lower than rutile in 6Mn-N-ZT-700, while the anatase reflex almost disappeared in 6Mn-N-ZT-900. The increasing calcination temperature beyond 500 °C causes the transformation of the crystalline phase from anatase to rutile [32].

Crystallite sizes of anatase TiO_2, rutile TiO_2 and tetragonal ZrO_2 in both 6Mn-N-ZT-700 and 6Mn-N-ZT-900 composites were calculated to observe any changes at different calcination temperatures. The (110) reflex of rutile was chosen to calculate the crystallite size. Table 3 summarizes the crystallite size of 6Mn-N-ZT-700 and 6Mn-N-ZT-900. The increasing crystallite size of rutile as the increasing calcination temperature indicates that higher calcination temperature beyond 700 °C promotes anatase-to-rutile phase transformation, in which it is higher than pristine TiO_2 (around 500 °C). The presence of ZrO_2 in the composite inhibits the crystallization of TiO_2.

Fig. 4 shows FTIR spectra of Mn-N-ZT-500 composite with various Mn contents; additionally, 6Mn-N-ZT calcined at 700 and 900 °C. FTIR spectra of all composites show hydroxyl (–OH) stretching vibration around 3300–3700 cm^{-1} and bending vibration around 1650 cm^{-1} [12]. The vibration at 1430 cm^{-1} indicates the presence of the O–N band that confirms the N atom in the TiO_2 network [33]. The vibration at the O–N bond plays an important role in the photocatalytic activity due

Table 3. Crystallite size of 6Mn-N-ZT calcined at 700 and 900 °C

Material	Crystal phase	D (nm)
6Mn-N-ZT-700	Anatase	59
	Rutile	46
	Tetragonal	35
6Mn-N-ZT-900	Rutile	69
	Tetragonal	38

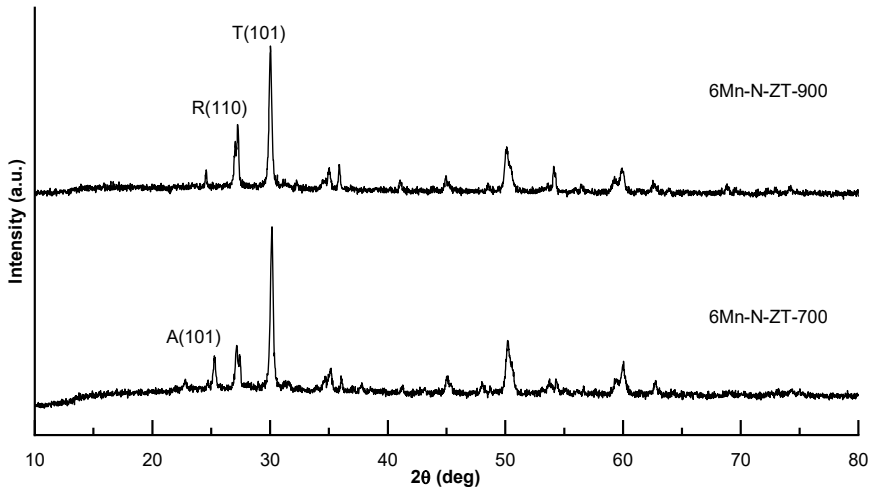

Fig 3. Diffraction patterns of 6Mn-N-ZT calcined at 700 and 900 °C whereas A, R and T represent anatase, rutile, and tetragonal crystal phases, respectively

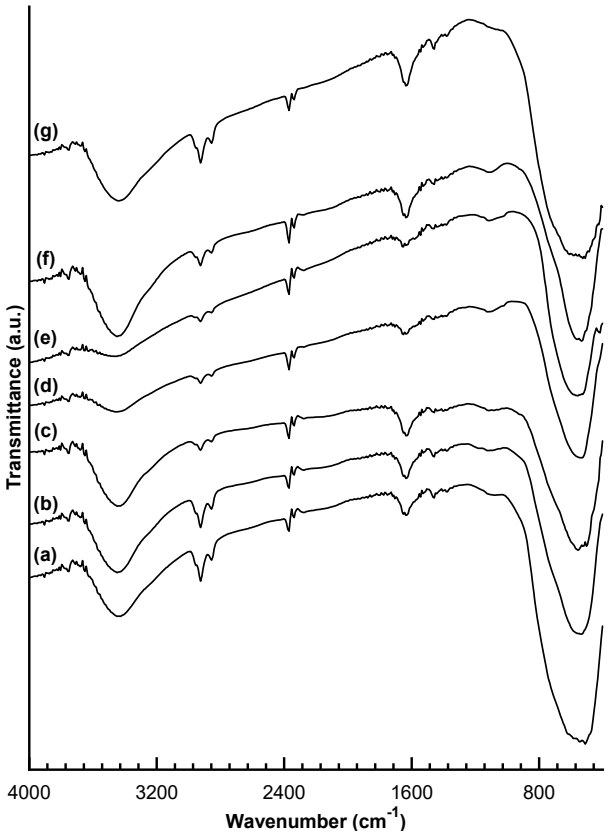

Fig 4. FTIR spectra of (a) 2Mn-, (b) 4Mn-, (c) 6Mn-, (f) 8Mn-, and (g) 10Mn-N-ZT-500, along with 6Mn-N-ZT (d) -700 and (e) -900

to the higher amount of surface-adsorbed water and hydroxyl groups [20]. An absorption spectrum at 1441 cm^{-1} region indicates the presence of Mn dopant in the composites [34]. At the low wavenumber region, the absorption belonged to the vibration of Ti–O–Ti, Mn–O–Ti, and Mn–O are found around 400–700 cm^{-1} [35]. Sharp peaks observed around 500 cm^{-1} correspond to the stretching vibration of Zr–O of the ZrO_2 phase [36]. Absorption spectra of Mn–O did not show any significant changes with the increasing Mn dopant content. The absorption intensity of the hydroxyl group decreases significantly as the calcination temperature increases beyond 500 °C. This is mainly due to the removal of water molecules from the sample and particle growth [36].

Fig. 5 presents the UV-Vis absorption spectral profiles of Mn-N-ZT composite with various Mn dopant contents and calcination temperatures, alongside TiO_2 500 °C and ZrO_2 500 °C as references. The calculated band gaps of Mn-N-ZT composites are summarized in Table 4. As shown in Fig. 5, the absorption edge of Mn-N-ZT-500 shifts to a longer wavelength as Mn dopant content increases from 2 up to 6%, but it shifts back to a shorter wavelength beyond 6 up to 10%. The pattern is similar to the band gap trends in Table 4.

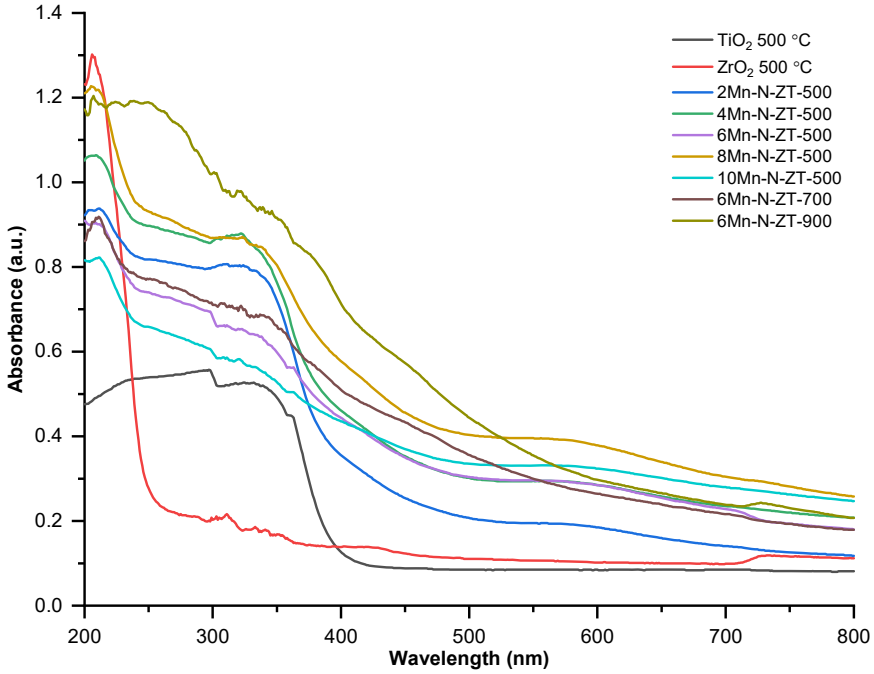

Fig 5. UV-Vis absorption spectra of various Mn-N-ZT with TiO_2 500 °C and ZrO_2 500 °C

Table 4. The calculated band gap of various Mn-N-ZT

Materials	Band gap (eV)
TiO_2 500 °C	3.20
ZrO_2 500 °C	4.91
2Mn-N-ZT-500	2.74
4Mn-N-ZT-500	2.67
6Mn-N-ZT-500	2.64
8Mn-N-ZT-500	2.71
10Mn-N-ZT-500	2.73
6Mn-N-ZT-700	2.51
6Mn-N-ZT-900	2.68

The addition of Mn dopants reduces the band gap to 2.64 eV until it reaches the optimum Mn content (6%). An excessive amount of metal dopants on the surface of TiO_2 can cause semiconductor-semiconductor heterojunction between the metal oxide and TiO_2 [37]. The band gap of 6Mn-N-ZT-700 (2.51 eV) is lower than 6Mn-N-ZT-500 (2.64 eV), while the band gap of 6Mn-N-ZT-900 is slightly higher (2.68 eV). High calcination temperature promotes the phase transformation of anatase to rutile in TiO_2. Rutile is the polymorph with the narrowest bandgap but mostly expresses up to an order of magnitude lower photocatalytic activity than anatase [38]. The band gap of 6Mn-N-ZT-900 is higher than 6Mn-N-ZT-700 due to the sintering of Mn at high calcination temperature, thus canceling the doping effect of Mn. All Mn-N-ZT composites possess a band gap in the range of visible light spectrum (less than 3.10 eV).

Fig. 6 shows the MB photodegradation percentage for various Mn-N-ZT at various times under visible light irradiation. All Mn-N-ZT composites display superior MB photodegradation percentage at 120 min compared to TiO_2 500 °C (9%) and ZrO_2 500 °C (5%). The percentage of MB degraded increases as the Mn dopant content increases to 6%, reaching up to 70% of MB 4 mg L^{-1} solution after 120 min irradiation. MB photodegradation percentage falls down as the amount of Mn dopant rises beyond 6%. The decline of MB photodegradation percentage also occurs in 6Mn-N-ZT-700 compared to 6Mn-N-ZT-500 and -900. Detailed photocatalytic activity of the composites represented as observed rate constant (k_{obs}) is shown in Fig. 7.

Based on k_{obs} data of all Mn-N-ZT-500 in Fig. 7, the photocatalytic activity increases up to 7.7 μg L^{-1} min^{-1} as the Mn dopant content increases up to 6%, then it declines to 5.4 μg L^{-1} min^{-1} as the Mn dopant content increases beyond 6%. It appears that the composite may agglomerate at higher dopant concentrations; therefore,

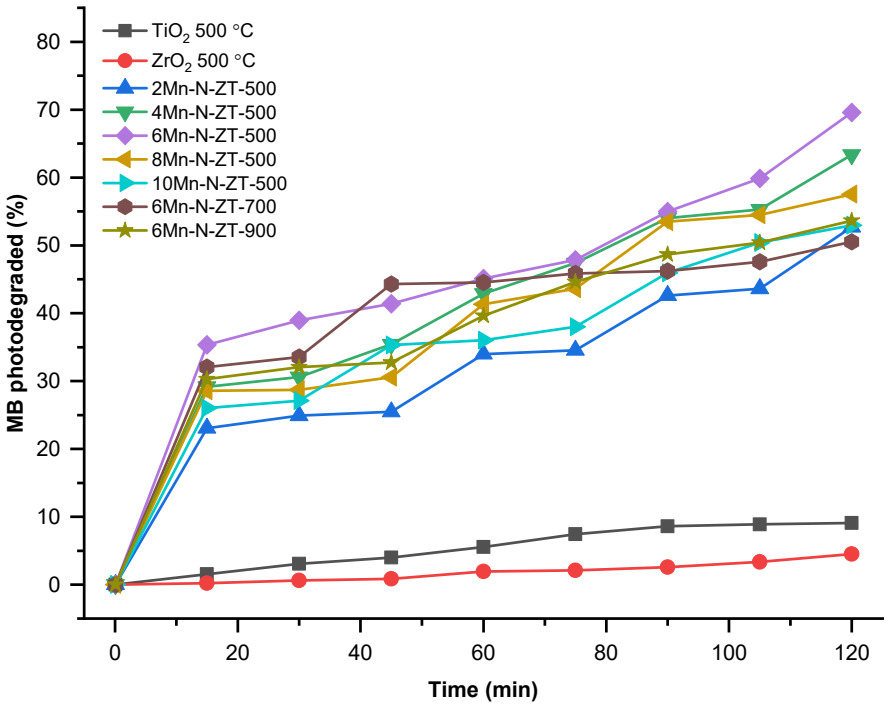

Fig 6. Percentage of photodegraded MB over time for various Mn-N-ZT

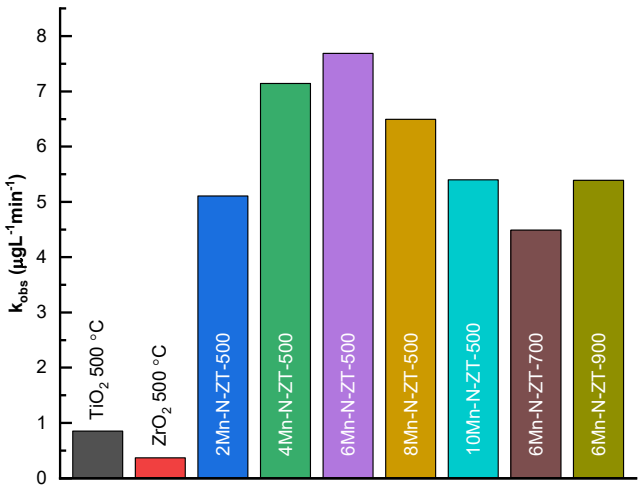

Fig 7. Summary of observed rate constant (k_{obs}) for various Mn-N-ZT

its surface is not fully exposed during photocatalysis [39]. The trend is similar to the band gap of Mn-N-ZT-500 with the increasing Mn contents. It indicates that the band gap constitutes the photodegradation properties of Mn-N-ZT-500. It is well known that the photocatalytic performance of a photocatalyst greatly depends on its electronic band structure because the band gap narrowing simultaneously weakens the redox power, either lowering the level of the conduction band or lifting the level of the valance band or both, which is detrimental to the photocatalytic capability [40]. On the contrary, 6Mn-N-ZT-700, with the lowest band gap, displays the lowest photocatalytic activity among other composites. The low band gap of 6Mn-N-ZT-700 and -900 is due to the presence of a rutile phase in the structure. The rutile phase is also known to demote the photocatalytic activity of TiO_2. The photocatalytic activity of all Mn-N-ZT composites under visible-light irradiation is significantly greater than TiO_2 500 °C and ZrO_2 500 °C. This phenomenon indicates that the coupling of ZrO_2-TiO_2 and codoping of Mn and N effectively improve photocatalytic performance.

■ CONCLUSION

Mn,N-codoped $ZrTiO_4$ composites with visible light photocatalytic properties have been prepared by the sol-gel method. The presence of Mn on the surface of the composite was confirmed by EDX analysis. Codoping with nitrogen and manganese shifts the band gap of the $ZrTiO_4$ composite down to 2.51 eV (6% Mn, 10% N, and calcination at 500 °C). The Mn,N-codoped $ZrTiO_4$ with 6% Mn and 10% N calcined 500 °C was able to degrade MB 4 mg L^{-1} solution up to 70% after 120 min irradiation under visible-light illumination, with observed rate constant (k_{obs}) of 7.7 µg L^{-1} min^{-1}. The Mn,N-codoped $ZrTiO_4$ is a potential photocatalyst for the photodegradation of methylene blue in an aqueous solution.

■ REFERENCES

[1] Siddeeg, S.M., Tahoon, M.A., Mnif, W., and Ben Rebah, F., 2019, Iron oxide/chitosan magnetic nanocomposite immobilized manganese peroxidase for decolorization of textile wastewater, *Processes*, 8 (1), 5.

[2] Zhu, C., Feng, Q., Ma, H., Wu, M., Wang, D., and Wang, Z., 2018, Effect of methylene blue on the properties and microbial community of anaerobic granular sludge, *BioResources*, 13 (3), 6033–6046.

[3] Khan, I., Saeed, K., Zekker, I., Zhang, B., Hendi, A.H., Ahmad, A., Ahmad, S., Zada, N., Ahmad, H., Shah, L.A., Shah, T., and Khan, I., 2022, Review on methylene blue: Its properties, uses, toxicity and photodegradation, *Water*, 14 (2), 242.

[4] Chung, K.T., Fulk, G.E., and Andrews, A.W., 1981, Mutagenicity testing of some commonly used dyes, *Appl. Environ. Microbiol.*, 42 (4), 641–648.

[5] Nasrullah, A., Khan, H., Khan, A.S., Man, Z., Muhammad, N., Khan, M.I., and Abd El-Salam, N.M., 2015, Potential biosorbent derived from *Calligonum polygonoides* for removal of methylene blue dye from aqueous solution, *Sci. World J.*, 2015, 562693.

[6] Yin, X., Liu, L., and Ai, F., 2021, Enhanced photocatalytic degradation of methylene blue by WO_3 nanoparticles under NIR light irradiation, *Front. Chem.*, 9, 683765.

[7] Han, M., Zhu, S., Lu, S., Song, Y., Feng, T., Tao, S., Liu, J., and Yang, B., 2018, Recent progress on the

photocatalysis of carbon dots: Classification, mechanism and applications, *Nano Today*, 19, 201–218.

[8] Huang, Z., Gao, Z., Gao, S., Wang, Q., Wang, Z., Huang, B., and Dai, Y., 2017, Facile synthesis of S-doped reduced TiO_{2-x} with enhanced visible-light photocatalytic performance, *Chin. J. Catal.*, 38 (5), 821–830.

[9] Koe, W.S., Lee, J.W., Chong, W.C., Pang, Y.L., and Sim, L.C., 2019, An overview of photocatalytic degradation: photocatalysts, mechanisms, and development of photocatalytic membrane, *Environ. Sci. Pollut. Res.*, 27 (3), 2522–2565.

[10] Zhang, J., Xiao, X., and Nan, J., 2010, Hydrothermal-hydrolysis synthesis and photocatalytic properties of nano-TiO_2 with an adjustable crystalline structure, *J. Hazard. Mater.*, 176 (1–3), 617–622.

[11] Reda, S.M., Khairy, M., and Mousa, M.A., 2020, Photocatalytic activity of nitrogen and copper doped TiO_2 nanoparticles prepared by microwave-assisted sol-gel process, *Arabian J. Chem.*, 13 (1), 86–95.

[12] Sudrajat, H., Babel, S., Ta, A.T., and Nguyen, T.K., 2020, Mn-doped TiO_2 photocatalysts: Role, chemical identity, and local structure of dopant, *J. Phys. Chem. Solids*, 144, 109517.

[13] Valero-Romero, M.J., Santaclara, J.G., Oar-Arteta, L., van Koppen, L., Osadchii, D.Y., Gascon, J., and Kapteijn, F., 2019, Photocatalytic properties of TiO_2 and Fe-doped TiO_2 prepared by metal organic framework-mediated synthesis, *Chem. Eng. J.*, 360, 75–88.

[14] Ganesh, I., Gupta, A.K., Kumar, P.P., Sekhar, P.S.C., Radha, K., Padmanabham, G., and Sundararajan, G., 2012, Preparation and characterization of Ni-doped TiO_2 materials for photocurrent and photocatalytic applications, *Sci. World J.*, 2012, 127326.

[15] Umar, K., Aris, A., Ahmad, H., Parveen, T., Jaafar, J., Majid, Z.A., Reddy, A.V.B., and Talib, J., 2016, Synthesis of visible light active doped TiO_2 for the degradation of organic pollutants—methylene blue and glyphosate, *J. Anal. Sci. Technol.*, 7 (1), 29.

[16] Negi, C., Kandwal, P., Rawat, J., Sharma, M., Sharma, H., Dalapati, G., and Dwivedi, C., 2021, Carbon-doped titanium dioxide nanoparticles for visible light driven photocatalytic activity, *Appl. Surf. Sci.*, 554, 149553.

[17] Khan, T.T., Rafiqul Bari, G.A.K.M., Kang, H.J., Lee, T.G., Park, J.W., Hwang, H.J., Hossain, S.M., Mun, J.S., Suzuki, N., Fujishima, A., Kim, J.H., Shon, H.K., and Jun, Y.S., 2021, Synthesis of N-doped TiO_2 for efficient photocatalytic degradation of atmospheric NOx, *Catalysts*, 11 (1), 109.

[18] Yu, W., Liu, X., Pan, L., Li, J., Liu, J., Zhang, J., Li, P., Chen, C., and Sun, Z., 2014, Enhanced visible light photocatalytic degradation of methylene blue by F-doped TiO_2, *Appl. Surf. Sci.*, 319, 107–112.

[19] Cravanzola, S., Cesano, F., Gaziano, F., and Scarano, D., 2017, Sulfur-doped TiO_2: Structure and surface properties, *Catalysts*, 7 (7), 214.

[20] Cheng, X., Yu, X., Xing, Z., and Yang, L., 2016, Synthesis and characterization of N-doped TiO_2 and its enhanced visible-light photocatalytic activity, *Arabian J. Chem.*, 9, S1706–S1711.

[21] Piątkowska, A., Janus, M., Szymański, K., and Mozia, S., 2021, C-,N- and S-doped TiO_2 photocatalysts: A review, *Catalysts*, 11 (1), 144.

[22] Długosz, O., Szostak, K., and Banach, M., 2020, Photocatalytic properties of zirconium oxide–zinc oxide nanoparticles synthesised using microwave irradiation, *Appl. Nanosci.*, 10 (3), 941–954.

[23] Zare, M.H., and Mehrabani-Zeinabad, A., 2022, Photocatalytic activity of $ZrO_2/TiO_2/Fe_3O_4$ ternary nanocomposite for the degradation of naproxen: characterization and optimization using response surface methodology, *Sci. Rep.*, 12 (1), 10388.

[24] Chandra, U., 2017, *Recent Applications in Sol-Gel Synthesis*, IntechOpen, Rijeka.

[25] Syoufian, A., and Nakashima, K., 2008, Degradation of methylene blue in aqueous dispersion of hollow titania photocatalyst: Study of reaction enhancement by various electron scavengers, *J. Colloid Interface Sci.*, 317 (2), 507–512.

[26] Hidayat, R., Wahyuningsih, S., Fadillah, G., and Ramelan, A.H., 2022, Highly visible light photodegradation of RhB as synthetic organic dye pollutant over TiO_2-modified reduced graphene

oxide, *J. Inorg. Organomet. Polym. Mater.*, 32 (1), 85–93.

[27] Muzammil, P., Basha, S.M., and Muhammed, G.S., 2020, Structural and magnetic properties of Fe-doped GaN by sol-gel technique, *J. Supercond. Novel Magn.*, 33 (9), 2767–2771.

[28] Feng, Z.H., Liu, B., Yuan, F.P., Yin, J.Y., Liang, D., Li, X.B., Feng, Z., Yang, K.W., and Cai, S.J., 2007, Influence of Fe-doping on GaN grown on sapphire substrates by MOCVD, *J. Cryst. Growth*, 309 (1), 8–11.

[29] Wolfgong, W.J., 2016, "Chemical Analysis Techniques for Failure Analysis: Part 1, Common Instrumental Methods" in *Handbook of Materials Failure Analysis with Case Studies from the Aerospace and Automotive Industries*, Eds. Makhlouf A.S.H., and Aliofkhazraei, M., Butterworth-Heinemann, Boston, 279–307.

[30] Titus, D., James Jebaseelan Samuel, E., and Roopan, S.M., 2019, "Nanoparticle Characterization Techniques" in *Green Synthesis, Characterization and Applications of Nanoparticles*, Eds., Shukla, Ashutosh K., and Iravani, S., Elsevier, Amsterdam, Netherlands, 303–319.

[31] Holzwarth, U., and Gibson, N., 2011, The Scherrer equation versus the 'Debye-Scherrer equation', *Nat. Nanotechnol.*, 6 (9), 534–534.

[32] Chauhan, R., Kumar, A., and Chaudhary, R.P., 2012, Structural and optical characterization of Zn doped TiO_2 nanoparticles prepared by sol-gel method, *J. Sol-Gel Sci. Technol.*, 61 (3), 585–591.

[33] Natarajan, T.S., Mozhiarasi, V., and Tayade, R.J., 2021, Nitrogen doped titanium dioxide (N-TiO_2): synopsis of synthesis methodologies, doping mechanisms, property evaluation and visible light photocatalytic applications, *Photochem*, 1 (3), 371–410.

[34] Sakthisharmila, P., Sivakumar, N., and Mathupriya, J., 2021, Synthesis, characterization of Mn, Fe doped ZrO_2 composites and its applications on photocatalytic and solar catalytic studies, *Mater. Today: Proc.*, 47, 2159–2167.

[35] Muslim, M.I., Kurniawan, R., Pradipta, M.F., Trisunaryanti, W., and Syoufian, A., 2021, The effects of manganese dopant content and calcination temperature on properties of titania-zirconia composite, *Indones. J. Chem.*, 21 (4), 882–890.

[36] Horti, N.C., Kamatagi, M.D., Nataraj, S.K., Wari, M.N., and Inamdar, S.R., 2020, Structural and optical properties of zirconium oxide (ZrO_2) nanoparticles: effect of calcination temperature, *Nano Express*, 1 (1), 010022.

[37] Sze, S.M., and Ng, K.K., 2006, *Physics of Semiconductor Devices*, 3rd Ed., Wiley-Interscience, Hoboken, New Jersey, US.

[38] Žerjav, G., Žižek, K., Zavašnik, J., and Pintar, A., 2022, Brookite vs. rutile vs. anatase: What`s behind their various photocatalytic activities?, *J. Environ. Chem. Eng.*, 10 (3), 107722.

[39] Zakria, H.S., Othman, M.H.D., Kamaludin, R., Sheikh Abdul Kadir, S.H., Kurniawan, T.A., and Jilani, A., 2021, Immobilization techniques of a photocatalyst into and onto a polymer membrane for photocatalytic activity, *RSC Adv*, 11 (12), 6985–7014.

[40] Chu, S., Wang, Y., Wang, C., Yang, J., and Zou, Z., 2013, Bandgap modulation of polyimide photocatalyst for optimum H_2 production activity under visible light irradiation, *Int. J. Hydrogen Energy*, 38 (25), 10768–10772.